Probing Causality of the Brainstem-Hypothalamic Murine Models of Sleep-Wake Regulation

Authors: Fatemeh Bahari[1,2]*, Myles W. Billard[1,2], John Kimbugwe[1,2], Carlos Curay[1], Glenn D.R. Watson[1,3], Kevin D. Alloway[1,3], Bruce J. Gluckman[1,2,4,5]*

Affiliations:

[1]Center for Neural Engineering, Pennsylvania State University, University Park, PA 16802, USA

[2]Department of Engineering Science and Mechanics, Pennsylvania State University, University Park, PA 16802, USA

[3]Neural and Behavioral Sciences, College of Medicine, Pennsylvania State University, Hershey, PA 17033, USA

[4]Department of Neurosurgery, College of Medicine, Pennsylvania State University, Hershey, PA 17033, USA

[5]Department of Bioengineering, Pennsylvania State University, University Park, PA 16802, USA

*Corresponding authors email addresses: Fatemeh Bahari, fa.bahari92@gmail.com, Bruce J. Gluckman BruceGluckman@psu.edu

Abstract

Sleep-wake regulation is thought to be governed by interactions among several nuclei in midbrain, pons, and hypothalamic regions. Determination of the causal role of these nuclei in state transitions requires simultaneous measurements from the nuclei with sufficient spatial and temporal resolution. We obtained long-term experimental single- and multi-unit measurements simultaneously from multiple nuclei of the putative hypothalamic and brainstem sleep-wake regulatory network in freely behaving rats. Cortical and hippocampal activity, along with head acceleration were also acquired to assess behavioral state. We found that although the average activity of cell groups during states matches the patterns presented previously in brief recordings of individual nuclei in head-fixed animals, the firing rates with respect to cortical and behavioral signs of state transitions differ in critical ways. Our findings pose fundamental questions about the neural mechanisms that maintain specific states and the neural interactions that lead to the emergence of new states.

Introduction

Sleep-wake states are thought to be driven by basal forebrain, brainstem, and hypothalamic circuits [1–8]. These states are predominantly characterized from electroencephalogram (EEG) and electromyogram (EMG) recordings, with transitions between states described as discrete mechanisms [4,9–12]. Models of underlying network mechanisms of sleep-wake regulation have attempted to describe and reproduce these discrete transitions [13–18]. To do so, these models often invoke co-inhibitory dynamics of sleep-wake regulatory cell groups in configurations analogous to electrical flip-flops [9,11,19]. However, observations of cell group activity and involvement are derived from experiments conducted on head-fixed [20–24] or lightly anesthetized animals [3,25], via short recordings, and often within novel environments [5,6,12,26–28]. These conditions inherently modulate sleep-wake patterns [29] and/or limit the time-resolution required for determination of the relationship between firing rate and state transitions. To investigate the neural basis of sleep-wake transitions in normal conditions, we chronically recorded single- and multi-unit activity simultaneously from multiple hypothalamic and brainstem sleep-wake regulatory nuclei in freely behaving rats. Cortical and hippocampal activity, along with head acceleration were also acquired to assess behavioral state. Here, we report a comprehensive network analysis of the sleep-wake regulatory system in freely behaving rats. Our findings address current hypotheses regarding the causal role of brainstem and hypothalamic cell groups in initiating naturally emerging transitions between states of vigilance.

Methods

All animal work was approved by and performed under the oversight of the Institutional Animal Care and Use Committee at the Pennsylvania State University.

To study the sleep-wake regulatory network as well as to identify sleep-wake transitions we used the systemDrive [30]: a customizable micro-wire multitrode microdrive for targeting multiple cell groups along non-parallel non-co-localized trajectories. Animals were implanted with the

systemDrive's micro-wire multitrodes targeting several sleep-wake regulatory cell-groups. The systemDrive houses additional screw electrodes for electrocorticography (ECoG), and fixed depth electrodes for hippocampal local field potential (LFP) recordings. Following implantation, animals were returned to their home-cages and long-term continuous recordings started after ample post-operation recovery time (7 days).

In accordance with common microdrive system use, we advanced electrodes along the dorsal-ventral axis of each targeted cell group and recorded neuronal activity of the area for continuous periods of 3 to 10 days. The procedure was repeated until the entire depth of the target was covered. Single- and/or multi-unit activity, when present, was extracted for all channels in each target. State of vigilance (SOV) was determined from simultaneous measurements of ECoG, hippocampal LFP, head acceleration [31], and time-matched video. The firing rate of each neuron was then analyzed as a function of different SOVs and their intervening transitions.

Animal Surgery and Care:

Surgical and implantation techniques are previously described [30]. Briefly, male and female Long Evans rats weighing between 275-350 grams were implanted for continuous recordings that lasted for a duration of 2-6 weeks.

Recording electrodes include micro-wire bundles for monitoring brainstem neuronal activity, as well as hippocampal LFP pairs and ECoG screws for determining the EEG and behavioral state. For observation of sleep-wake regulatory network (SWRN) dynamics, we recorded from five brainstem structures with target coordinates referenced to intraural line (IA) according to the Paxinos-Watson rat brain atlas:

Dorsal Raphe (DR) [AP: +1.5 mm, ML: 0 mm, DV: -3.6 mm, 21.33^{o} or -21.33^{o}]

PeduncloPontine Tegmentum (PPT) [AP: +0.5 mm, ML: ±2 mm, DV: -3.6 mm]

LateroDorsal Tegmentum (LDT) [AP: +0.36 mm, ML: ±0.8 mm, DV: -3 mm, 13.65^{o} or -13.65^{o}]

VentroLateral Preoptic Area (VLPO) [AP: +8.76 mm, ML: ±1 mm, DV: -0.75 mm, 15.52^{o}]

Locus Coerleus (LC) [AP: -0.72 mm, ML: +1.3 mm, DV: -3.2 mm]

A number of these nuclei are located near sensitive structures such as the sagittal sinus and lateral ventricles. Therefore, trajectories were chosen to avoid these sensitive structures and allow enough room on the cranium for all electrodes.

For hippocampal LFPs, two pairs of custom-made 50 µm iridium oxide deposited micro-reaction chamber (µRC) electrodes formed from gold coated stainless-steel wire [32] with ends staggered by 250-300 µm were implanted bilaterally in the dorsal hippocampus at coordinates [AP: +5 mm, ML: ±3 mm, DV: -2.5 mm from the cortex]. For ECoG, four stainless steel screws (one-eighth inch 18-8 stainless steel 0-80 cortical screws, McMaster-Carr) were implanted at coordinates [AP: +7.5 mm, ML: ±4 mm], [AP: +3 mm, ML: -4 mm], and [AP: +2.5 mm, ML: +3 mm]. Two additional stainless screws were implanted at [AP: +11 mm, ML: ±3 mm] for ground and reference.

After completing surgery, animals were returned to their individual home-cages for recovery with free access to food and water. Following recovery, the animals were cabled for continuous video and EEG monitoring. Every 3 to 10 days the animals were briefly anesthetized to advance the micro-wire electrodes incrementally between recording sessions and until they covered the entire dorsal-ventral length of the structures of interest.

Histological Techniques:

At the completion of recordings animals were sacrificed and their brains were histologically processed to examine the electrode tracks with respect to the targeted brain structures. Details and results of the histological methods and analysis are previously described [30].

Data Acquisition:

All rats were housed individually in custom-made plexiglass cages with dimensions 9” (w) x 15” (d) x 24” (h). At the first electrode driving session, each animal received a differential

or referential digitizing head-stage amplifier with 3-axis accelerometer (RHD2116 or RHD2132, Intan Technologies, Los Angeles, CA) which can directly connect to an electrode interface board on the systemDrive. The amplifier was connected to a data acquisition board (RHD2000 Evaluation System, Intan Technologies) via 3' lightweight serial-peripheral interface (SPI) cable (Intan Technologies) and in-house adapted low-torque commutator (SRA-73540-12, Moog Inc.).

Hippocampal LFP, ECoG, as well as single and multi-unit signals were simultaneously acquired at 30,000 samples per second (SPS) and high-pass filtered at 1 Hz. Head acceleration measurements were sampled at a rate of 7500 Hz. A 12 hour light/dark cycle was maintained with the lights on between 6 am and 6 pm. Video monitoring, at 3 frames per second, began on the day of implantation and continued within each recording session. Video files were stored in one-hour-long files, while biopotentials and head acceleration data were stored in 5 to 15-minute-long files for further analysis.

To measure single- and multi-unit activity we used the microdrive arrangements within the systemDrive. For each animal, electrodes aimed at sleep-wake regulatory cell-groups in the brainstem and/or hypothalamus were first advanced after the recovery period.

During this and subsequent driving sessions, the animal was maintained under anesthesia with 0.5%-2% isoflurane gas and the head-mount was opened to access the systemDrive. We maintained the recordings throughout the driving session. Each electrode bundle was advanced incrementally (about 25μm) and the signal was monitored until we observed new single-unit activity. For electrode trajectories that passed through the superior and inferior colliculi or other sensory-responsive regions, we tested auditory and visual stimuli to evoke responses that would confirm that the electrode was advancing through the appropriate brain structures.

Data Analysis:

All analyses were performed using custom-written MATLAB (Mathworks) and Labview (National Instruments) scripts.

Sleep and Behavioral Scoring:

Hippocampal LFP, ECoG, and accelerometer time-series were down-sampled to 1000 samples per second and reformatted into 1 hour-long blocks of binary data within a custom Labview script. The raw data were then band-pass filtered at 1-125 Hz for LFP, 1-55 Hz for ECoG, and 2-100 Hz for head acceleration.

SOV was marked using an adaptation of the semi-automatic Linear Discriminant Analysis (LDA) within custom-written Labview scripts previously described [31,33]. The SOV was initially classified into four main states: Non-rapid eye movement (NREM) sleep, rapid eye movement (REM) sleep, awake ($wake_{wb}$), and active exploration with non-coherent theta rhythm ($wake_{\theta}$). For each animal, 4-6 hours of video-EEG data within 1 day were randomly selected and manually scored for SOV and SOV transition time. These data were then used to train the LDA. The remaining 18-20 hours of data were set aside as out-of-sample data (test set). For both training and test sets, features were computed, within 2 second long windows, from EEG spectral power in frequency bands 0.5-4, 4-8, 8-12, 12-25, and 25-80 Hz, plus coherence measurements and head acceleration. The features were generated using causal filters and updated every second at the end of computation window. Therefore, all the scores are based on information up to the time leading to the state transition and *not* after that.

We further introduced Bayesian probabilities for each state given its previous state. For example, REM normally occurs after NREM. Exceptions to this are in Narcolepsy and sleep deprivation [34]. We verified the performance of the classifier for out-of-sample test data and used the classified SOV as the new training set to recursively update the parameters of the LDA.

Head acceleration and EEG spectral power have been widely used to distinguish between discrete states of NREM, REM, $wake_{wb}$, and $wake_{\theta}$. For instance, changes in theta to delta power ratio is commonly used to mark transitions between NREM and REM. As the animal transitions from NREM to REM the decrease in delta power and appearance of theta power will increase the

$\frac{\theta}{\delta}$ ratio. Theta rhythm is also expressed during exploratory wake bouts, which are at times associated with small movement marked by exploratory whisking. $Wake_{\theta}$ bouts could be mislabeled by the $\frac{\theta}{\delta}$ ratio. However, the theta rhythm in the REM state is much more spatially coherent than in $wake_{\theta}$. Therefore we used temporal coherence in one hippocampal channel and spatial coherence between hippocampal channels of the theta band to further distinguish REM bouts. After identification of the intermediate state (IS) (see Results) we updated the process for the LDA-based automatic sleep-scoring to include IS based on the same features.

Spike Scoring:

We used Intan Technologies differential (RHD2216) and referential (RHD2132) preamplifiers to acquire electrophysiological signals. The default pass-band for the filters in these preamplifiers is between 0.1 Hz and 7.5 kHz. A 16-bit analog to digital converter then samples the signal from the AC-coupled amplifiers. At 7.5 kHz, the cut-off frequency in the analog low-pass filter is much higher than what is used conventionally (e.g. 3.5 kHz in [12,23]).

Data segments were filtered with a causal band-pass filter with 250 Hz to 7.5 kHz pass-band, and then thresholded to detect single-unit activity. Units were detected as instances of threshold crossings where thresholds were specified as multiples of the standard deviation of the filtered background signals. The background signals represent separate epochs of time that are free of distinguishable spiking activity and are used to calculate the mean and variance of the background distribution. We detected units with a threshold of 5-7 standard deviations. When spike events were detected, the waveform of each action potential was extracted from the data.

Statistical Analysis:

The core analysis of this work is to characterize the state-dependent firing rate for each neuron, and determine the times with respect to observed state transitions, when the neuron changes firing rate from its pre-transition baseline firing rate.

We adopted the Poisson process statistics for calculations of the instantaneous firing rate and statistical comparisons to determine the time point at which a significant change in firing rate happens (t_{sig}):

$$P_\lambda(k) = \frac{\lambda^k e^{-\lambda}}{k!}, \qquad \lambda = FR \times N \times \boldsymbol{\tau}$$

Where FR is the instantaneous state-dependent firing rate, N is the number of trials, τ is the bin size, and λ is the mean state-dependent firing rate. The "trials" here are relevant state transitions, i.e. firing rate of a PPT REM-active neuron during IS to REM transitions (Fig. S1).

For each neuron and each identified state transition (e.g. NREM to REM), the pre-transition mean firing rates (λ) over many trials (e.g. NREM bouts) form the reference Poisson distribution. We then used the cumulative distribution function with 1%-99% confidence intervals to find the post-transition instantaneous firing rate outside of the confidence bounds. The time point associated with the significantly different instantaneous firing rate was then determined as t_{sig}.

During the course of our experiments, the activity of each neuron at each target location was measured over many sleep-wake cycles (n = 100-300). The large ensemble of "trials" enables us to have sub-second resolution (bin size) in our statistical analysis, which is crucial for causality determination.

Results

We successfully acquired simultaneous measurements from up to four separate sleep-wake regulatory nuclei (SWRN) in each rat. The success rates of chronic systemDrive targeting and recording from multiple (n = 12) rats are shown in Table S1. Each target was categorized by whether the electrode tracks reached the target SWRN, and whether unit activity characteristic of those nuclei were recorded. Cumulative recording duration, number of recording sessions, and number of single units exceeding a threshold of 7 standard deviations are presented for each

animal. The extended 3-10 day recording sessions generally began when the electrodes were estimated to be in their target structures. Each successive recording session had at least one of the electrode bundles at a new ventral location within the targets.

A distinct intermediate state exists between non-rapid eye movement sleep and rapid eye movement sleep

A transitional stage prior to REM was first described by Gottesmann [35] in Wistar rats. They found that REM was often preceded by simultaneous high-amplitude cortical spindles – EEG sign of NREM – and hippocampal theta activity – EEG sign of REM. The group later characterized the transitional stage using multi-unit recordings from the pontine reticular formation and a distribution of cortical and hippocampal electrodes, and coined the name “Intermediate State” [36,37].

We observed the intermediate state (IS) in our measurements and identified it as a spectrally distinct extended state that often occurred at the end of NREM. The time and frequency features of IS during a NREM to REM transition are illustrated in Fig. 1. NREM is associated with slow (1-4 Hz), large amplitude cortical oscillations (red panel in Fig. 1A). In contrast, REM is characterized by rhythmic theta (5-8 Hz) in both hippocampus and cortex (green panel in Fig. 1A). IS onset is defined by appearance of weak bursts of theta-band activity in the presence of identifiable, although weaker than in NREM, delta band activity. IS termination is defined by a large reduction of power in the slower delta band and a sharp increase in the theta band power, often indicating the onset of REM. During the IS (onset and offset marked by magenta lines in Fig. 1A), the head acceleration power is low with no evidence of the short spikes characteristic of muscle twitches during REM. Unlike NREM and REM states that have clear spectral peaks in the delta and theta bands, the IS simultaneously exhibits broader power peaks covering delta and higher theta frequencies (Fig. 1B). Further, the theta oscillations during IS are both temporally and spatially incoherent.

To visualize moment-to-moment transitions in sleep-wake states, we used the canonical discriminant space of the LDA. Because points in the LDA space represent brain activity at different times, we can link the consecutive points to illustrate trajectories. These trajectories passing through different clusters then represent transitions between states. The 2-D projection of the full canonical space onto the first two canonical discriminant coordinates is shown in Fig. 1C. We calculated the iso-probability contours in the 2-D space and used them to mark the boundaries of each state. The onset and offset of trajectories that describe transitions through states were then marked as crossings of the boundaries. Overlaid on the clusters in Fig. 1C are representative trajectories between NREM and wake as well as NREM and REM. We found that within the 2-D LDA space, an overwhelming number of trajectories from NREM to REM and NREM to wake appear to dwell and pass through the well-defined cluster corresponding to the IS.

Once we quantified the transition probabilities for all possible state transitions (Fig. 1D), we found that in all transitions out of NREM, 40% merged into IS. Further, 80% of the transitions out of IS merged into REM, while the remaining 20% transitioned to the wake state.

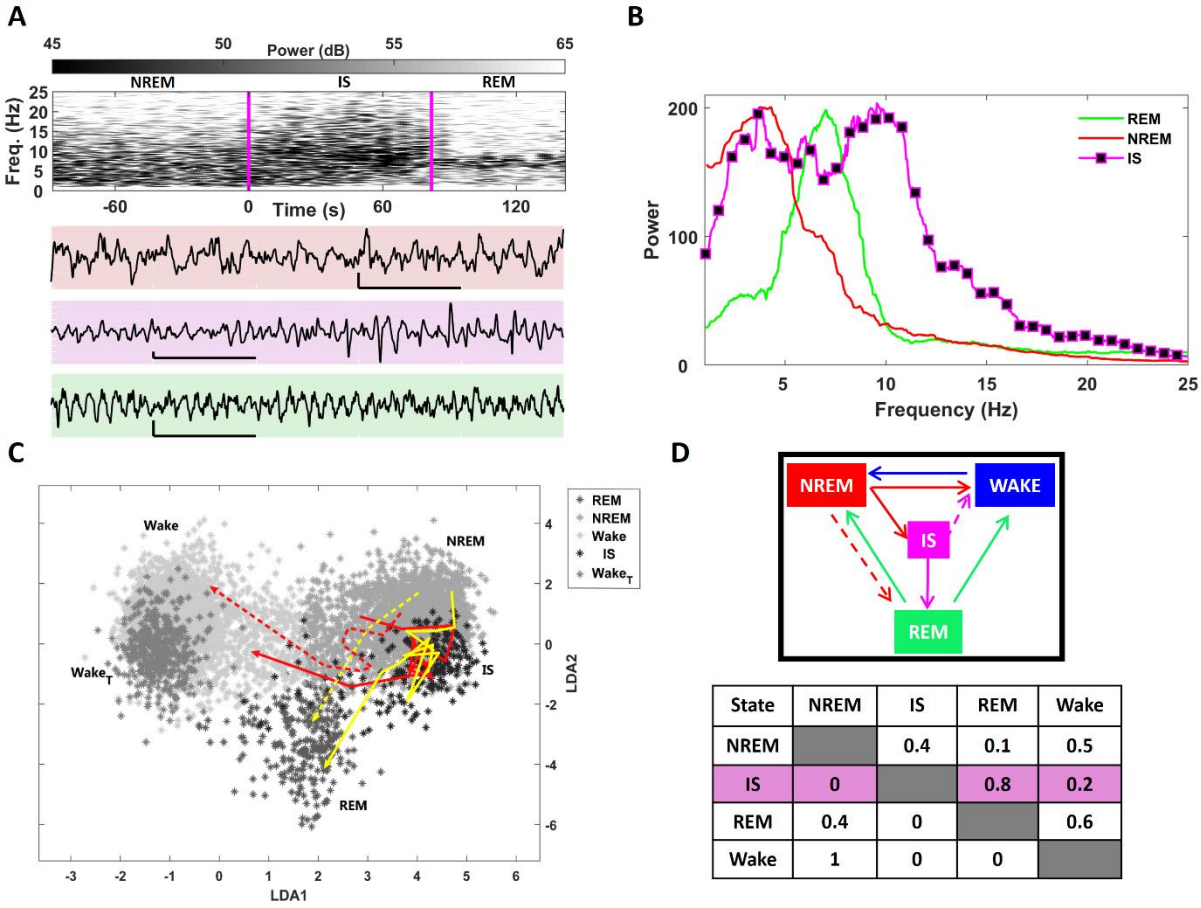

State	NREM	IS	REM	Wake
NREM		0.4	0.1	0.5
IS	0		0.8	0.2
REM	0.4	0		0.6
Wake	1	0	0	

Figure 1. Time-frequency characteristics of the intermediate state (IS). **(A)** Hippocampal LFP recording illustrating spectral power fluctuations during NREM to IS to REM transitions. As the brain exits NREM, spectral power increases in the theta range simultaneous with persisting power in the delta range. The REM onset is then marked by a striking increase of coherent activity in the theta range. The IS onset and end are marked by solid magenta lines. All vertical and horizontal scale bars are 100 mV and 1 second; respectively. Power is calculated over 8 second windows with 4 second overlap and normalized to 0.001 as base-power. **(B)** The simultaneous delta and theta activity in the IS is highlighted in the power plot averaged over 20 second long time-series for each state. Power is calculated from the hippocampal LFP recording channel as in **A** with overlapping 2 s long windows. **(C)** Scatter plot of the first two linear canonical discriminants highlight the five groups: NREM, REM, IS, Wake, or $Wake_T$ ($wake_{theta}$). We define the transitions between states as trajectories connecting the clusters in the canonical space. Typical direct trajectories from NREM to REM and NREM to Wake are illustrated in dashed yellow

and red arrow-lines. Most transitions from NREM to REM pass through the IS region (solid yellow line). A few transitions from NREM to Wake pass through the IS region (solid red line). **(D)** The transition probabilities between possible SOVs. Because majority of transitions from NREM to REM pass the IS region, direct transitions are marked by a red dashed line.

Characterization of the intermediate state during light/dark cycle

In diurnal animals, such as rats, most of the light period is spent in fragmented sleep with few wake bouts and most of the dark period is spent in fragmented wake with few sleep bouts. The mean and standard deviations of hourly fractions spent in each SOV, including the IS, pooled across all 12 animals used in this study are shown in Fig. 2A. Green denotes REM, magenta denotes IS, red denotes NREM, and blue denotes wake. The light/dark (L/D) cycle is shown by color, where yellow indicates light and gray indicates dark periods.

Collectively, wake accounts for 45 to 55% of the time. NREM accounts for majority of time in sleep, corresponding to 35 to 40% of the day. REM sleep occurs for the small fraction of 5-10% of the day. These patterns all display clear diurnal variations. The IS, regardless of its next state (either wake or REM), accounts for ~2-4% of the time during the dark period and ~2-6% of the time during the light period (Fig. 2C). As shown in Fig. 2B, regardless of the time of day (TOD), IS lasts sufficiently to be detectable with our sleep-scoring algorithm.

Only 20% of the transitions out of IS merged into the wake state. We investigated whether the IS epochs that merged into wakefulness are different from the ones that transitioned to REM. We found that the duration of IS prior to wake is on average higher than the duration of IS prior to REM. We used survival analysis to investigate whether the duration of IS bouts could be used to distinguish bouts that transition to REM from bouts that transition to wake. Within our experiments, failure is defined as a transition out of IS, into either REM or Wake. In contrast, we define survival as remaining in IS. IS bouts pooled across all 12 animals were scored for duration and marked as either IS to REM or IS to wake. We then calculated the survival, failure, and cumulative incidence functions as well as the hazard rates for both groups. The hazard rates, $\lambda_{IS,\ Transition\ Type}$, for IS to REM and IS to wake transitions are shown in Fig. 2D. The hazard functions have different scales, with $\lambda_{IS,\ wake}$ on average 4 times higher than $\lambda_{IS,\ REM}$. This 4:1 ratio is consistent with the post-IS SOV distribution in the dataset. The shape of the hazard functions for the IS to REM and

IS to wake groups are also different. The $\lambda_{IS, REM}$ first grows and then quickly decays at 70 s. The IS bouts longer than 70 s all transition to wake. The $\lambda_{IS, wake}$ remains comparatively flat with a small peak at a longer IS duration of 80 seconds which corresponds to the maximum IS duration we found in the dataset.

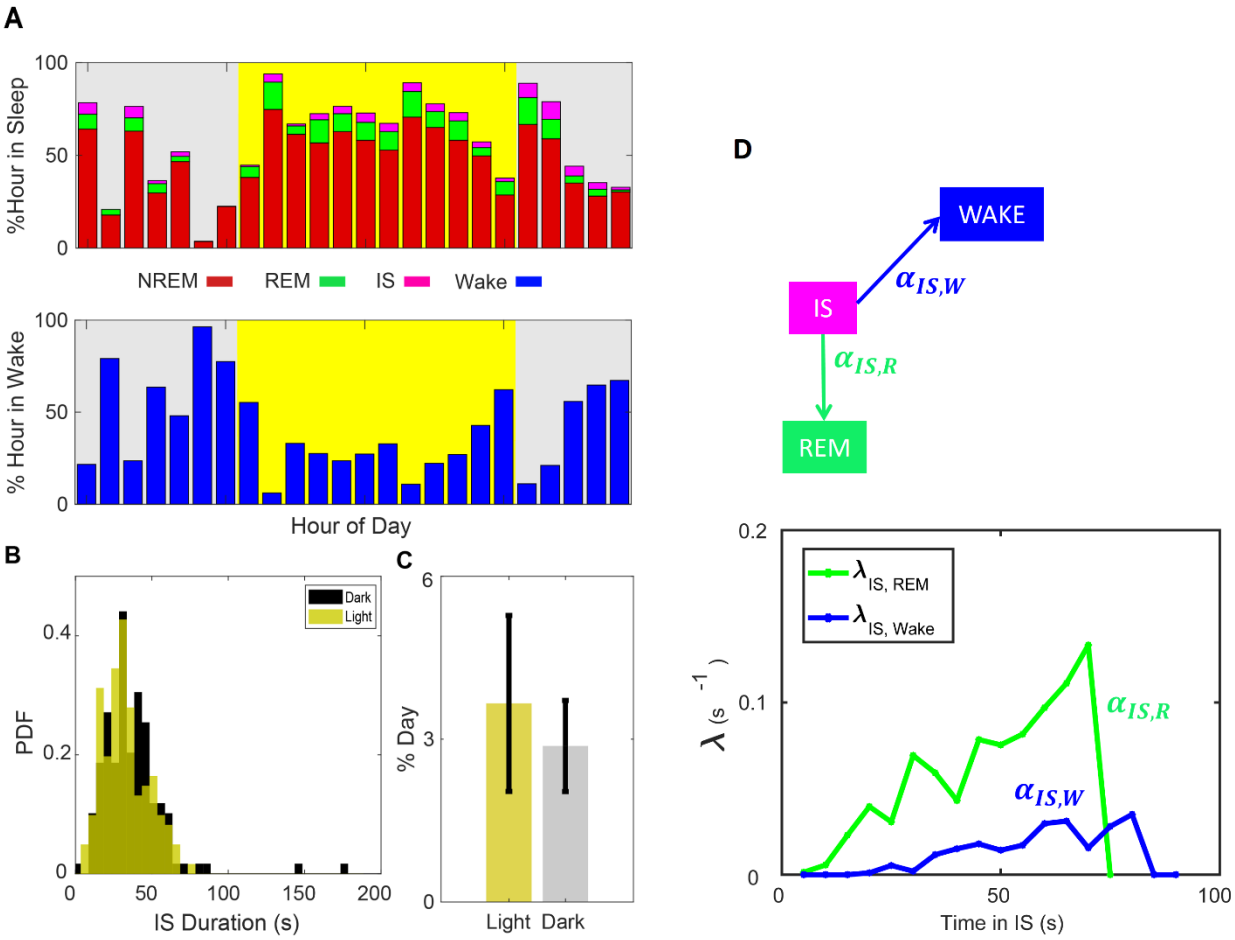

Figure 2. IS patterns and duration across the light/dark cycle. (**A)** Hourly percentages spent in NREM (red), IS (magenta), REM (green), and Wake (blue) are shown for all the recorded rats. Most of the light period (background yellow) is spent in sleep and most of the dark period (background gray) is spent in Wake. **(B)** Distribution of the duration of the IS pooled from all animals during both light and dark periods. Regardless of the time of day, the intermediate state lasts for a considerable amount of time that should be detectable in the current sleep-scoring algorithms. **(C)** Mean and standard deviation of percent of time spent in IS for light and dark period. **(D)** IS bouts pooled across all rats (n=13) were scored as either IS → REM or IS → Wake.

297 Hazard rates were calculated using competing groups. Competing groups analysis assumes one
298 event precludes the other. $\lambda_{IS,\ REM}$ is on average 4 times larger than $\lambda_{IS,\ wake}$. This ratio indicates
299 the relative frequency of REM and Wake transition types in the data set. The $\lambda_{IS,\ REM}$ first grows
300 and then quickly decays, with peaks at IS duration of 30 and 70 seconds. $\lambda_{IS,\ wake}$ remains
301 comparatively flat with a small peak at 80.

302

Mean state-dependent neuronal firing rate of the brainstem-hypothalamic SWRN

Our experiments here were motivated by the brainstem-hypothalamic mechanism of sleep-wake regulation. In this model interactions between cholinergic PPT/LDT, monoaminergic LC/DR, and GABAergic VLPO lead to different SOVs. Cumulatively, we recorded 855 single units across multiple regions and many continuous days (3-10 days) from 12 freely behaving animals all in their home-cage environment. A range of 100-300 complete sleep cycles were recorded from each neuron. Half (n = 428) of the identified single-units recorded were SOV-dependent: 170 were REM-active, 15 were NREM active, 142 were wake-active, 60 were wake and REM active, and 41 were active in all SOVs except REM (denoted as REM-off). These neurons were distributed throughout multiple brain regions: We found Wake-active neurons in PPT, LDT, and DR; NREM-active neurons in VLPO; REM-active neurons in PPT, LDT, and in lateral hypothalamus adjacent to VLPO. We also identified a group of REM-off neurons located in vlPAG.

The mean firing rate of each identified SOV-dependent neuron during each SOV is shown in Fig. 3A. The firing rates for each neuronal group, during different SOVs, are separated based on light (orange dots) and dark cycles (blue dots). For each neuronal group the firing rates are normalized to the maximum firing rate of the group over all SOVs (M_{FR}) shown in black dots. The neuronal groups are separated by neuron type, as defined by a combination of anatomical location, SOV-dependence, and the waveform pattern of the extracellular action potential. Representative average waveforms by type are shown in Fig. 3B.

We found that the maximum firing rates of neurons in each neuronal group within each state formed substantially low variance distributions and were highly consistent across states. This indicates a level of homogeneity in state-dependent firing rate for each neuronal group. Further, the mean and maximum state-dependent firing rates for each neuronal group (Fig. 3A) were consistent with previous reports of state-dependent neuronal activity in different cell groups of the

sleep-wake regulatory network [12,21,23,28]. We therefore interpret this set of data as an ensemble representative of the dynamics of these cell-group activities.

Out of the represented neuronal groups, VLPO is one of the most challenging structures for continuous stable recordings. This explains the dearth of reports of continuous electrode recordings, and the fact that such recordings, when available, are performed in short bouts or when the animal's movements are restricted [28]. To our knowledge, we are the first to report consistent multi-day observations of VLPO neuronal activity that enabled calculations of mean state-dependent firing rates during NREM.

The mean state-dependent firing rate of a subset of neuronal groups was slightly different during light versus dark periods. These included the wake-REM active neurons of PPT and LDT and the REM-off neurons of vlPAG. However, for most of the groups we did not find a consistent circadian difference in mean state-dependent firing rates.

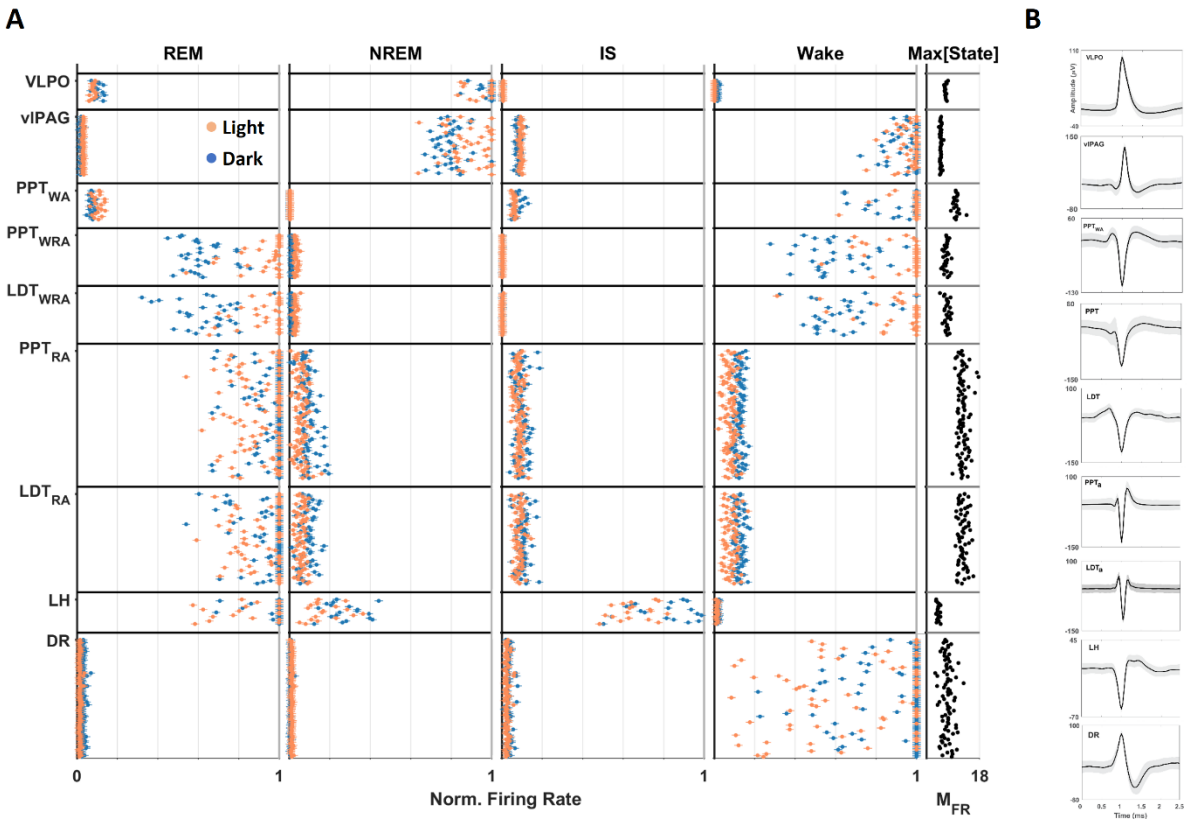

Figure 3. Mean and standard deviation of the firing rates of all recorded neurons in brainstem-hypothalamic sleep-wake regulatory network. (A) Firing rates of state-dependent neurons whose recording sites were histologically confirmed pooled from all recording days across all animals. The firing rate of each neuron is marked by orange for the light period and blue for the dark period. For each neuron the firing rate is normalized to the maximum firing rate of that neuron across all states of vigilance. The maximum firing rate for each neuron is illustrated on the right by black dots in the Max[State] column. In PPT and LDT we found a variety of neurons that were REM-active (RA), Wake and REM active (WRA), or Wake active (WA). The neurons are separated here based on their location and activity dependence. The average state-dependent firing rates appear to be extremely consistent across all neurons and states. **(B)** Representative average waveforms for all neuronal groups.

VLPO, ventrolateral preoptical area; vlPAG, ventrolateral periacquaductal gray; PPT, pedunculopontine tegmentum; LDT, laterodorsal tegmentum; LH, lateral hypothalamus; DR, dorsal raphe.

Neurons in lateral hypothalamus are active during IS

As shown in Fig. 3A, none of the identified state-dependent neurons active during NREM, REM, or wake states were active during the IS. However, we identified a group of IS-active neurons in the lateral preoptic area (Fig. S2A). Based on their activity profile (Fig. S2B), spike waveform (Fig. S2C), and ventral location, these neurons might be the GABAergic melatonin concentrating hormone (MCH) neurons distributed in lateral hypothalamus that were formerly identified as REM-active neurons [24,38–40].

As shown in Fig. S2B these neurons have high discharge rates during REM as well as IS bouts and are almost silent during NREM and wake. EEG activity in the theta band is a mutual feature of both IS and REM states. This might imply that the IS-active neurons of LH are linked to theta band activity rather than a specific SOV. However, we found that the discharge rate of these neurons was remarkably low during active exploration ($Wake_{\theta}$) bouts which are associated with theta band activity in EEG. The IS can therefore be characterized as a distinct SOV with clear EEG and behavioral signs as well as corresponding neuronal activity.

We found no significant difference between average discharge rate of these neurons during IS bouts prior to Wake versus the IS bouts prior to REM.

Investigation of causality of neuronal activity in emergence of cortical signs of SOV

We aimed to investigate the role of brainstem and hypothalamic neurons in the emergence of SOVs and transitions between them. By analyzing the temporal relationship between spontaneous neuronal activity and state transitions in freely behaving animals, we can clarify the role of any given cell-group in initiating or maintaining a SOV. The question is whether the activity of any given neuron precedes or follows the SOV transitions.

The SOV and state transition times, as described in the methods, were defined from the hippocampal, cortical, and behavioral signs of the state [7] using causal spectral features of the hippocampal LFP, ECoG, and head acceleration. These features were updated every second at

379 the end of the computation window, hence allowing for almost instantaneous determination of
380 SOV. This contrasts sharply with conventional methods of sleep-scoring with non-overlapping
381 windows of fixed length (e.g. 4 s in mice, 10 s in rats) that are attributed a score for the full length
382 of the window rather than the state onset.

383 Neuronal firing rates over many sleep cycles (~100-300) were derived from simultaneous
384 measurements of single-unit activity from a subset of the SWRN. For each SOV transition (from
385 state A to B), we collected the distribution of firing rates while in state A. The firing rate was
386 calculated from spike-times separated from state transitions by at least (3 seconds)). The
387 transition time (t_{trans}) was defined as the time when EEG and behavioral signs of state B first
388 emerged. Following the Poisson process statistics (see Methods) we determined the time-point
389 that the instantaneous state-conditioned firing rate during state B differed significantly from the
390 firing rate in state A. The time-point is denoted as t_{sig}. The large ensemble of firing rates for each
391 neuron during each transition (sleep-wake cycles = 100-300) allows for sub-second resolution
392 determination of t_{sig}.

393 If the significant change in the state-conditioned firing rate occurred prior to transition time
394 $t_{sig} < t_{trans}$, then it is counted as negative t_{sig}. Positive t_{sig} indicates that the state-conditioned firing
395 rate changed after transition time, $t_{sig} > t_{trans}$. A positive t_{sig} implies that the changes in firing of that
396 neuron type cannot be causal for the state transition.

397 The t_{sig} values for the 428 identified state-dependent neurons are marked by blue dots in Fig. 4.
398 The gray shading indicates the positive t_{sig} and therefore non-causal relationships. The white
399 shading indicates the negative t_{sig} where the change in firing rate occurred prior to state transition.
400 For each cell group and state transition, dashed gray lines indicate the representative average
401 state-dependent firing rate as a function of time during state transitions. We found that the t_{sig}
402 values for individual cells are tightly distributed within each cell group for each state transition.
403 This indicates the consistency of neuronal activity during state transitions.

Cell groups whose mean firing rates increase during state transitions (e.g. REM-active PPT or LDT neurons during NREM to REM transitions) can either turn on to cause the state ($t_{sig} < 0$, white shading in Fig. 4), which means high discharge rates prior to emergence of cortical signs of a SOV, or can be turned on as a consequence of state transition ($t_{sig} > 0$, gray shading in Fig. 4). Among all cell groups with increasing firing rate during state transitions, only NREM-active neurons of VLPO and REM-off neurons of vlPAG during REM to NREM transitions had negative t_{sig}. The discharge rate of all other neurons increases *after* the appearance of EEG and behavioral signs of SOV. Therefore, the increase in their discharge rate does not mean that they are causing the state change, only that their behavior is a consequence of the state change.

Likewise, cell groups whose mean firing rate decreases during state transitions (e.g. wake-active DR neurons during wake to NREM transitions) can either be responsible for the emergence of the state ($t_{sig} < 0$, white shading in Fig. 4), or be inhibited as a consequence of the state ($t_{sig} > 0$, gray shading in Fig. 4). We found that all the cell groups that decreased their firing rates during state transitions did so prior to transition time ($t_{sig} < 0$), which could allow a new SOV to emerge. Whether this pattern is internally sourced by the cell groups or by an external signal remains unknown.

The NREM-active neurons of VLPO are the only population with negative t_{sig} values during all state transitions. Specifically, during transitions into NREM the activity of the VLPO neurons increases significantly with respect to the state-conditioned average firing rate prior to the state transition. These neurons also decrease their firing rate significantly prior to transitions out of NREM. Therefore, the causality hypothesis [4,8] holds for the NREM-active neurons of VLPO.

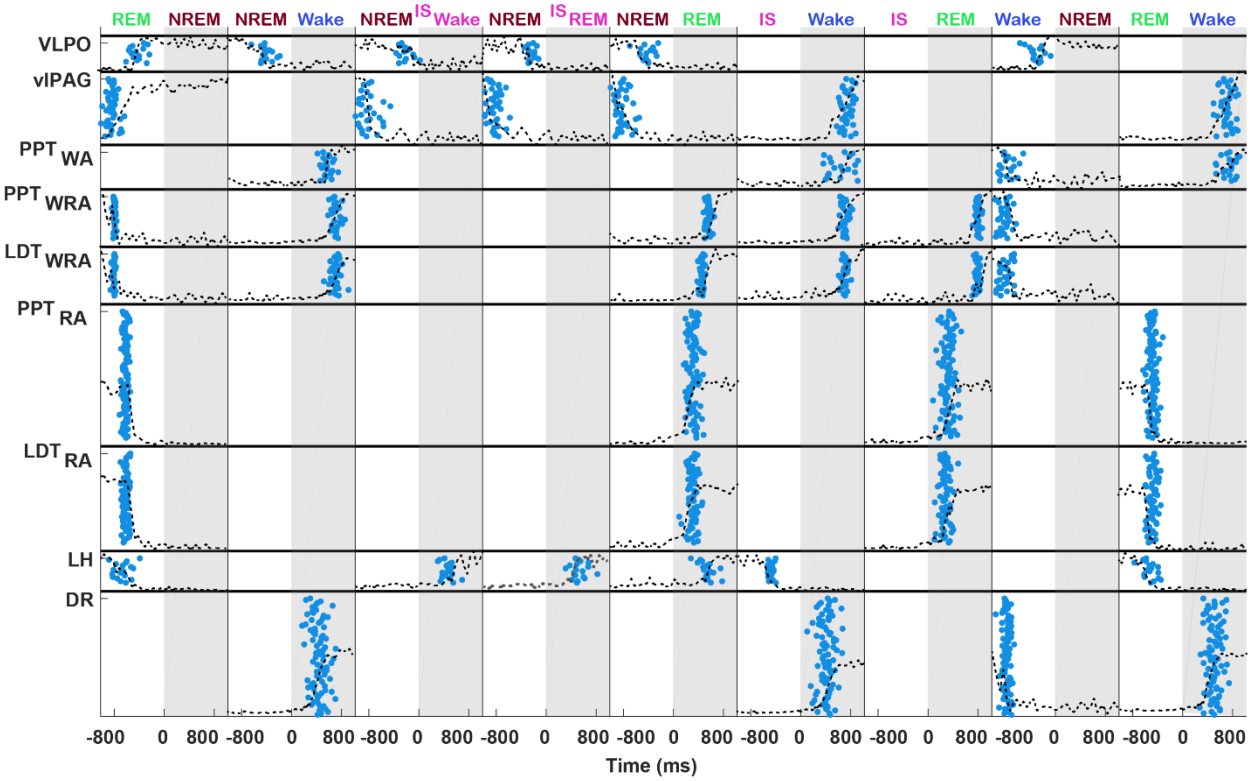

425

426 **Figure 4. The t_{sig} for all neurons with respect to cortically defined state transitions.** Each column
427 indicates a state transition, where the transition is marked by time zero. The state before and
428 after the transitions are marked by the white and gray backgrounds, respectively. The t_{sig} for
429 each neuron is indicated by a blue dot. Representative average firing rates during transition are
430 shown by the dashed gray lines. The firing rates for DR, PPT/LDT_{RA}, PPT/LDT_{WRA} groups are
431 normalized to half height of the plot box. Other firing rates are normalized to the full height of
432 the plot box. Notice that for every neuronal group and transition, the t_{sig} values are tightly
433 distributed. This indicates that the activity of these neurons is extremely consistent. The gray
434 shading indicates the positive t_{sig} and not causal relationships while the white areas are negative
435 t_{sig} indicating that the neuron changed its behavior prior to the appearance of cortical signs of a
436 state.

437 VLPO, ventrolateral preoptical area; vlPAG, ventrolateral periacquaductal gray; PPT,
438 pedunculopontine tegmentum; LDT, laterodorsal tegmentum; LH, lateral hypothalamus; DR,
439 dorsal raphe.

440

NREM-active and REM-active neurons demonstrate distinct dynamics during IS

Because we found that IS seems to be characteristic of ending of NREM and often precedes REM, we utilized the t_{sig} values to investigate the behavior of REM and NREM active neurons during IS transitions. During NREM to IS transitions, the discharge rates of both the solely NREM-active neurons of VLPO and the REM-off neurons of vlPAG decreased prior to transition into IS ($t_{sig} < 0$). The behavior of NREM-active neurons implies a level of causality, but whether the decrease in firing rate is programmed internally or caused by other factors remains to be investigated. In contrast, the discharge rate of the REM-active as well as REM and wake active neurons of PPT and LDT does not change during NREM to IS transitions, i.e. their firing rate remains just as low during IS as during NREM.

We found a population of neurons in lateral hypothalamus that were active during both REM and IS. These neurons remained active with no substantial change in their firing rate during IS to REM transitions. During transitions out of REM to NREM or wake, these neurons decreased their firing rate prior to the transition time ($t_{sig} < 0$). Likewise, the firing rate decreased prior to the transitions out of IS to wake ($t_{sig} < 0$). We did not find a causal increase in firing rate during NREM to IS transitions ($t_{sig} > 0$). The increase in firing rate appeared to be following the emergence of IS rather than causing it.

Nonetheless, the activity of the NREM-active neurons during transitions into IS and the activity of the IS-active LH neurons during the IS indicates that the IS is a distinct state of vigilance rather than only a transitory dynamic between NREM and REM.

Discussion

We developed a dataset including 569 cumulative days of SOV-scored single- and multi-unit measurements from multiple cell-groups in the sleep-wake regulatory network (SWRN). These

466 measurements are from 12 freely behaving rodents, with each rat recorded for over 30 day
467 periods, which consisted of multiple segments of continuous recordings that lasted 3 to 10 days.
468 To our knowledge this is the most detailed SOV scored dataset of long-term and simultaneous
469 measurements of single-unit activity from multiple of the brainstem and hypothalamic cell groups;
470 PPT, LDT, DR, LH, vlPAG, and VLPO in freely behaving rodents.

471 Our dataset complements previous work [4,7,11,20,21,23,25,28,41,42] , but is characterized by several
472 significant distinctions.

473 First, our simultaneous measurements of hippocampal LFP, ECoG, head acceleration, and
474 neuronal activity from multiple cell-groups in freely behaving animals represent a novel “systems
475 neuroscience" attempt aimed at characterizing the dynamics of the brainstem-hypothalamic
476 SWRN system described by Saper et al. [4,9]. Second, the data include continuous measurements
477 from NREM-active VLPO neurons over many (100-300) consecutive sleep-cycles without
478 introduction of any restrictions to affect animal behavior. Third, our approach to sleep scoring
479 resulted in continuous and temporally precise determination of SOV and SOV transition times.
480 Fourth, time-resolved analysis of the SOV and SOV transition times as well as acquisition of
481 sufficient sleep-wake cycles provide suitable statistical power to probe causality between
482 neuronal firing rates and emergence of cortical signs of states. Finally, we re-discovered the
483 intermediate state (IS, see [43]) and characterized it as a distinct state that usually follows NREM
484 and precedes REM. Furthermore, we identified neurons in lateral hypothalamus (LH) that become
485 active during the IS.

486 Much of the research investigating the neuronal activity of the cell-groups in the SWRN is
487 performed within conditions that inherently modulate the animals’ sleep cycles and/or limit the
488 time-resolution required for determination of the relationship between firing rate and state
489 transitions. Almost all sleep studies available today are performed with head-fixed animals, or in
490 novel environments such as isolation boxes, and provide short recordings of the sleep cycles.

While such methods avoid the technical challenges associated with simultaneously recording the hippocampal, cortical, and behavioral indices of different sleep states as wells as state-dependent neuronal activity, they complicate the analysis of SWRN dynamics.

Deviations from normal home-cage environments change the animals' normal behavior and sleep-wake cycles. Short-term recordings from restricted animals eliminate the effect of exogenous (light-dark cycles) and endogenous circadian cycles on sleep dynamics. Furthermore, to detect a statistically significant change in neuronal firing rates during state transitions, with sub-second temporal resolution, many sleep cycles are required. Finally, conventional SOV scoring techniques assign a score to non-overlapping time-windows with fixed length and predetermined boundaries. These fixed windows prevent accurate assessment of the SOV dynamics and identification of the true onset of a state.

Implications of the intermediate state for sleep-wake regulation

Gottesmann was the first to identify an intermediate state in Wistar rats that occurred between NREM and REM, and which exhibited both cortical spindles (a sign of NREM) and hippocampal theta rhythm (a sign of REM) [35] . Gottesmann's finding of the IS was also confirmed in other rat experiments [43–45] and observed in humans by Lairy et al [46]. In humans, the IS was characterized as a short EEG stage (a few seconds to a few minutes) with spindles and K complexes (signs of slow wave sleep, stage 2), and low voltage activity without eye movement (sign of paradoxical sleep) [46]. More recently this state has appeared in a small subset of publications focused on more accurate sleep-scoring algorithms [47] and sleep irregularities in neurological disorders [48,49]. However, despite Gottesmann's findings and characterizations of it, the intermediate state has not been considered a formal state of vigilance.

We re-discovered the IS in our animals and found distinct temporal, spectral, and neuronal patterns associated with it that identify it as a formal SOV. The IS lasts for a considerable amount of time (median duration = 35 s, Fig. 2B) that should be detectable in current sleep-scoring

algorithms. The spectral features of the IS are distinct from both NREM and REM and although IS often follows NREM, we never observed transitions from IS back to NREM. Therefore, IS cannot be categorized as short fluctuations of cortical activity during transitions out of NREM. Moreover, we found specific neurons in LH that are active during IS while other REM- or NREM-active neurons are off during the state. We, therefore, identify the IS as a distinct state of vigilance.

The conventional/routine sleep-scoring analyses assume state transitions are discrete and easily classified by fast changes in EEG features, and in behavioral and physiological activity represented by EMG power, head acceleration, heart rate, and/or breathing. The states are often identified as NREM, REM, and Wake (both active exploratory wake and quiet wake)[9]. Therefore, research has focused on identifying brain regions involved in triggering discrete transitions between these states. However, the emergence of relatively enduring (35 s on average) EEG spectral characteristics that combine and expand upon the features of both NREM and REM in the transition from NREM to REM or to wakefulness indicates that conclusions regarding the mechanisms underlying the onset of any SOV must be revisited.

The technical challenges in measuring from a number of SWRN nuclei indicate the value of SWRN mathematical models (see for example [16,17]) for understanding the underlying mechanisms of sleep-wake regulation. However, the models and the experiments they are based on have generally not considered the existence of the IS or the unique sets of IS-active neurons. Implementation of the IS as a distinct SOV with its own state-active neurons will enable the models to provide mechanistic insight into differentiation between transitions to Wake versus transitions to REM.

The IS-active neurons in lateral hypothalamus remained active during IS to REM transitions. However, these neurons turned off prior to transitions out of IS and into wake. Therefore, we hypothesize that the activity of these LH neurons determines whether transitions out of IS progress into REM or wake. Lateral hypothalamus and basal forebrain have been recently

implicated in sleep-wake regulation [5,39], and these neurons and their activity profile motivate further probing of that circuit.

Implications of correlative vs. causal activity in the brainstem-hypothalamic SWRN

We used time-resolved transition-based analysis to probe the causality of the SWRN dynamics in transitions between states of vigilance. With the exception of NREM-active VLPO neurons, increases in state-conditioned mean firing rate always followed the emergence of the state which is determined from cortical and behavioral signs. An increase in neuronal activity that follows the SOV cannot be programming it.

Datta et al. [12] investigated the role of cholinergic PPT neurons in REM regulation. They scored states of vigilance in 10 s epochs and used a combination of muscle atonia, rapid eye movement, and hippocampal theta waves to mark REM state. They found that 9 out of 70 PPT neurons recorded exhibited high firing rates during REM. Previously it had been shown that PPT lesions result in immediate reduction of REM [9]. Datta et al. concluded that PPT neurons are involved in both the induction and the maintenance of REM from NREM sleep and are a precursor to the signs of REM [7].

In agreement with Datta et al. observations, we observed that PPT activity increases during REM. However, we observed increased PPT activity only *after* emergence of cortical signs of REM and not prior to it. This questions the hypothesized role of cholinergic REM-on PPT neurons in REM induction. We suspect that this mismatch is due to two factors. First, the spectral and temporal features used in our sleep-scoring are generated via causal filters and updated every second at the end of computation window. Therefore, all the scores are based on information up to the time leading to the state transition and *not* after that. This is in contrast to fixed length windows used in conventional sleep-scoring that are susceptible to missing the correct transition time. Second, for each neuron we collected a large ensemble of firing rates computed over many sleep-wake

565 cycles. The large sample size enables sub-second resolution in determining transition-based
566 changes in firing rate (see Methods).

567 We observed a similar behavior for other identified SWRN nuclei. Neurons in REM-active LDT,
568 Wake/REM-active PPT and LDT, Wake-active DR, Wake-active PPT, and REM-off vlPAG cell
569 groups all show a significant change in their firing rate only *after* their corresponding state
570 transitions.

571 The cell groups involved in sleep-wake regulation are functionally and spatially heterogeneous
572 and extend across large neural territories. The presence of such a large number of variable cell
573 groups that are implicated in the control of the brain's arousal state poses questions on how they
574 interact to govern rapid ultradian transitions within a sleep cycle (i.e. NREM to REM) as well as
575 much slower homeostatic and circadian processes. While acute disruptions of the interactions
576 within the SWRN via anatagonist injections or optogenetic inhibition cause acute loss of the
577 corresponding SOV, chronic ablation of the basal forebrain cholinergic neurons [50], the
578 tuberomammillary histaminergic neurons [51], the LC and pontine cholinergic neurons [26,52,53], or
579 combinations of these structures [54] have minimal effects on the regulation of that SOV.

580 Further, almost all of the SWRN brain regions contain intermingled cell types that are active during
581 more than one SOV. For example in the basal forebrain, glutamatergic, cholinergic, and
582 parvalbumin (PV)-expressing GABAergic neurons are shown to be active during both REM and
583 wake, but their optogenetic activation promotes only wakefulness [5]. This raises the question as
584 to which cell group is involved in maintaining a state rather than specifically initiating the switch
585 into that state.

586 Logically, a routine based on acute study of stimulus (lesion/optogenetics)-response (i.e. changes
587 to SOV length and occurrence) dynamics might not be fitting for investigation of a naturally
588 occurring spontaneous behavior such as sleep-wake transition and cycling. Therefore, although

589 internal/external stimuli might cause transitions into a state, it does not necessarily mean that the
590 stimulated neurons are causal for the emergence of the state in normal conditions.

591 Our findings indicate that the long-standing flip-flop model of sleep-wake regulation [4] needs
592 significant revision. Fundamental questions remain about the neural mechanisms that maintain
593 specific states and the neural interactions that lead to the emergence of new states.

594

References

1. Moruzzi, G. & Magoun, H. W. Brain stem reticular formation and activation of the EEG. *Electroencephalogr. Clin. Neurophysiol.* (1949). doi:10.1016/0013-4694(49)90219-9

2. ECONOMO, C. V. SLEEP AS A PROBLEM OF LOCALIZATION. *J. Nerv. Ment. Dis.* **71**, 249–259 (1930).

3. Sherin, J. E., Elmquist, J. K., Torrealba, F. & Saper, C. B. Innervation of Histaminergic Tuberomammillary Neurons by GABAergic and Galaninergic Neurons in the Ventrolateral Preoptic Nucleus of the Rat. *J. Neurosci.* (2018). doi:10.1523/jneurosci.18-12-04705.1998

4. Saper, C. B., Fuller, P. M., Pedersen, N. P., Lu, J. & Scammell, T. E. Sleep State Switching. *Neuron* (2010). doi:10.1016/j.neuron.2010.11.032

5. Xu, M. *et al.* Basal forebrain circuit for sleep-wake control. *Nat. Neurosci.* **18**, 1641–1647 (2015).

6. Weber, F. *et al.* Control of REM sleep by ventral medulla GABAergic neurons. *Nature* (2015). doi:10.1038/nature14979

7. Datta, S. & MacLean, R. R. Neurobiological mechanisms for the regulation of mammalian sleep–wake behavior: reinterpretation of historical evidence and inclusion of contemporary cellular and molecular evidence. *Neurosci. Biobehav. Rev.* **31**, 775–824 (2007).

8. Saper, C. B., Scammell, T. E. & Lu, J. Hypothalamic regulation of sleep and circadian rhythms. *Nature* **437**, 1257–1263 (2005).

9. Saper, C. B., Chou, T. C. & Scammell, T. E. The sleep switch: Hypothalamic control of sleep and wakefulness. *Trends in Neurosciences* (2001). doi:10.1016/S0166-2236(00)02002-6

10. Luppi, P.-H. *et al.* Paradoxical (REM) sleep genesis: the switch from an aminergic–cholinergic to a GABAergic–glutamatergic hypothesis. *J. Physiol.* **100**, 271–283 (2006).

11. Weber, F. & Dan, Y. Circuit-based interrogation of sleep control. *Nature* (2016). doi:10.1038/nature19773

12. Datta, S. & Siwek, D. F. Single cell activity patterns of pedunculopontine tegmentum neurons across the sleep-wake cycle in the freely moving rats. *J. Neurosci. Res.* **70**, 611–621 (2002).

13. Phillips, A. J. K. & Robinson, P. A. Sleep deprivation in a quantitative physiologically based model of the ascending arousal system. *J. Theor. Biol.* **255**, 413–423 (2008).

14. Fulcher, B. D., Phillips, A. J. K. & Robinson, P. A. Modeling the impact of impulsive stimuli on sleep-wake dynamics. *Phys. Rev. E* **78**, 51920 (2008).

15. Rempe, M. J., Best, J. & Terman, D. A mathematical model of the sleep/wake cycle. *J. Math. Biol.* **60**, 615–644 (2010).

16. Tamakawa, Y., Karashima, A., Koyama, Y., Katayama, N. & Nakao, M. A quartet neural system model orchestrating sleep and wakefulness mechanisms. *J. Neurophysiol.* **95**, 2055–2069 (2006).

17. Fleshner, M., Booth, V., Forger, D. B. & Diniz Behn, C. G. Circadian regulation of sleep–wake behaviour in nocturnal rats requires multiple signals from suprachiasmatic nucleus. *Philos. Trans. R. Soc. A Math. Phys. Eng. Sci.* **369**, 3855–3883 (2011).

18. Diniz Behn, C. G. & Booth, V. Simulating Microinjection Experiments in a Novel Model of the Rat Sleep-Wake Regulatory Network. *J. Neurophysiol.* **103**, 1937–1953 (2010).

19. Lu, J., Sherman, D., Devor, M. & Saper, C. B. A putative flip–flop switch for control of REM sleep. *Nature* **441**, 589–594 (2006).

20. Takahashi, K., Kayama, Y., Lin, J. S. & Sakai, K. Locus coeruleus neuronal activity during the sleep-waking cycle in mice. *Neuroscience* (2010). doi:10.1016/j.neuroscience.2010.06.009

21. Boucetta, S., Cisse, Y., Mainville, L., Morales, M. & Jones, B. E. Discharge Profiles across the Sleep-Waking Cycle of Identified Cholinergic, GABAergic, and Glutamatergic Neurons in the Pontomesencephalic Tegmentum of the Rat. *J. Neurosci.* **34**, 4708–4727 (2014).

22. Boissard, R. *et al.* The rat ponto-medullary network responsible for paradoxical sleep onset and maintenance: a combined microinjection and functional neuroanatomical study. *Eur. J. Neurosci.* **16**, 1959–1973 (2002).

644 23. Sakai, K. Sleep-waking discharge profiles of dorsal raphe nucleus neurons in mice. *Neuroscience*
645 **197**, 200–224 (2011).

646 24. Verret, L. *et al.* A role of melanin-concentrating hormone producing neurons in the central
647 regulation of paradoxical sleep. *BMC Neurosci.* (2003). doi:10.1186/1471-2202-4-19

648 25. Aston-Jones, G., Chen, S., Zhu, Y. & Oshinsky, M. L. A neural circuit for circadian regulation of
649 arousal. *Nat. Neurosci.* **4**, 732–738 (2001).

650 26. Lu, J. Identification of Wake-Active Dopaminergic Neurons in the Ventral Periaqueductal Gray
651 Matter. *J. Neurosci.* (2006). doi:10.1523/jneurosci.2244-05.2006

652 27. Bjorness, T. E. *et al.* An Adenosine-Mediated Glial-Neuronal Circuit for Homeostatic Sleep. *J.*
653 *Neurosci.* **36**, 3709–3721 (2016).

654 28. Alam, M. A., Kumar, S., McGinty, D., Alam, M. N. & Szymusiak, R. Neuronal activity in the preoptic
655 hypothalamus during sleep deprivation and recovery sleep. *J. Neurophysiol.* **111**, 287–299 (2014).

656 29. Sigl-Glöckner, J. & Seibt, J. Peeking into the sleeping brain: Using in vivo imaging in rodents to
657 understand the relationship between sleep and cognition. *Journal of Neuroscience Methods*
658 (2019). doi:10.1016/j.jneumeth.2018.09.011

659 30. Billard, M. W., Bahari, F., Kimbugwe, J., Alloway, K. D. & Gluckman, B. J. The systemDrive: a
660 Multisite, Multiregion Microdrive with Independent Drive Axis Angling for Chronic Multimodal
661 Systems Neuroscience Recordings in Freely Behaving Animals. *eneuro* **5**, ENEURO.0261-
662 18.2018 (2018).

663 31. Sunderam, S. *et al.* Improved sleep-wake and behavior discrimination using MEMS
664 accelerometers. *J. Neurosci. Methods* **163**, 373–383 (2007).

665 32. Shanmugasundaram, B. & Gluckman, B. J. Micro-reaction chamber microelectrodes especially for
666 neural and biointerfaces. (2017).

667 33. Sedigh-Sarvestani, M. *et al.* Rapid eye movement sleep and hippocampal theta oscillations
668 precede seizure onset in the tetanus toxin model of temporal lobe epilepsy. *J. Neurosci.* **34**, 1105–

14 (2014).

34. Chemelli, R. M. *et al.* Narcolepsy in orexin Knockout Mice. *Cell* **98**, 437–451 (1999).

35. Gottesmann, C. Données sur l'activité corticale au cours du sommeil profond chez le rat. *CR Soc. Biol.(Paris)* **158**, 1829–1834 (1964).

36. Terrier, G. & Gottesmann, C. L. Study of cortical spindles during sleep in the rat. *Brain Res. Bull.* **3**, 701–6 (1978).

37. Gandolfo, G., Glin, L. & Gottesmann, C. Study of sleep spindles in the rat: A new improvement. *Acta Neurobiol. Exp. (Wars).* (1985).

38. Jego, S. *et al.* Optogenetic identification of a rapid eye movement sleep modulatory circuit in the hypothalamus. *Nat. Neurosci.* (2013). doi:10.1038/nn.3522

39. Tsunematsu, T. *et al.* Optogenetic Manipulation of Activity and Temporally Controlled Cell-Specific Ablation Reveal a Role for MCH Neurons in Sleep/Wake Regulation. *J. Neurosci.* (2014). doi:10.1523/jneurosci.5344-13.2014

40. Apergis-Schoute, J. *et al.* Optogenetic Evidence for Inhibitory Signaling from Orexin to MCH Neurons via Local Microcircuits. *J. Neurosci.* **35**, 5435–5441 (2015).

41. Cox, J., Pinto, L. & Dan, Y. Calcium imaging of sleep–wake related neuronal activity in the dorsal pons. *Nat. Commun.* **7**, 10763 (2016).

42. Van Dort, C. J. *et al.* Optogenetic activation of cholinergic neurons in the PPT or LDT induces REM sleep. *Proc. Natl. Acad. Sci.* (2015). doi:10.1073/pnas.1423136112

43. GOTTESMANN, C. The Transition from Slow-wave Sleep to Paradoxical Sleep: Evolving Facts and Concepts of the Neurophysiological Processes Underlying the Intermediate Stage of Sleep. *Neurosci. Biobehav. Rev.* **20**, 367–387 (1996).

44. Neckelmann, D., Olsen, O. E., Fagerland, S. & Ursin, R. The reliability and functional validity of visual and semiautomatic sleep/wake scoring in the Moll-Wistar rat. *Sleep* (1994).

693 doi:10.1093/sleep/17.2.120

694 45. Gandolfo, G., Romettino, S., Gottesmann, C., Van Luijtelaar, G. & Coenen, A. Genetically epileptic
695 rats show a pronounced intermediate stage of sleep. *Physiol. Behav.* **47**, 213–215 (1990).

696 46. Lairy, G. C. Données récentes sur la physiologie et la physiopathologie de l'activité onirique.
697 Données EEG chez le malade mental. *IV World Congr. Psychiatry* **1**, 189–197 (1966).

698 47. Gervasoni, D. Global Forebrain Dynamics Predict Rat Behavioral States and Their Transitions. *J.*
699 *Neurosci.* **24**, 11137–11147 (2004).

700 48. Pitkänen, A., Ekolle Ndode-Ekane, X., Lapinlampi, N. & Puhakka, N. Epilepsy biomarkers –
701 Toward etiology and pathology specificity. *Neurobiology of Disease* (2019).
702 doi:10.1016/j.nbd.2018.05.007

703 49. Andrade, P., Nissinen, J. & Pitkänen, A. Generalized Seizures after Experimental Traumatic Brain
704 Injury Occur at the Transition from Slow-Wave to Rapid Eye Movement Sleep. *J. Neurotrauma*
705 (2017). doi:10.1089/neu.2016.4675

706 50. Kaur, S., Junek, A., Black, M. A. & Semba, K. Effects of Ibotenate and 192IgG-Saporin Lesions of
707 the Nucleus Basalis Magnocellularis/Substantia Innominata on Spontaneous Sleep and Wake
708 States and on Recovery Sleep after Sleep Deprivation in Rats. *J. Neurosci.* (2008).
709 doi:10.1523/jneurosci.1585-07.2008

710 51. Gerashchenko, D., Chou, T. C., Blanco-Centurion, C. A., Saper, C. B. & Shiromani, P. J. Effects of
711 Lesions of the Histaminergic Tuberomammillary Nucleus on Spontaneous Sleep in Rats. *Sleep* **27**,
712 1275–1281 (2004).

713 52. Webster, H. H. & Jones, B. E. Neurotoxic lesions of the dorsolateral pontomesencephalic
714 tegmentum-cholinergic cell area in the cat. II. Effects upon sleep-waking states. *Brain Res.* (1988).
715 doi:10.1016/0006-8993(88)90471-4

716 53. Shouse, M. N. & Siegel, J. M. Pontine regulation of REM sleep components in cats: integrity of the
717 pedunculopontine tegmentum (PPT) is important for phasic events but unnecessary for atonia

during REM sleep. *Brain Res.* **571**, 50–63 (1992).

54. Blanco-Centurion, C., Gerashchenko, D. & Shiromani, P. J. Effects of Saporin-Induced Lesions of Three Arousal Populations on Daily Levels of Sleep and Wake. *J. Neurosci.* **27**, 14041–14048 (2007).

Supplementary Material

Animal # (Sex)	Days Recorded [# of Sessions]	PPT		LDT		DR	LC	VLPO
		Left	Right	Left	Right			Right
1 (M)	41 [13]					47 (23)		
2 (M)	37 [12]	42 (21)	33 (13)			43 (17)		
3 (M)	57 [9]	29 (19)	29(8)			18 (10)		
4 (M)	73 [12]	7 (1)				18 (7)		
5 (M)	66 [10]	20 (9)			14 (4)	27 (10)		
6 (M)	43 [8]	24 (20)			29 (22)	32 (11)		26 (10)
7 (F)	39 [7]		6 (4)	19 (12)		3 (2)		9 (4)
8 (F)	54 [9]	K			47 (28)	44 (31)		
9 (M)	57 [9]	8 (6)			43 (21)	23 (3)		13 (5)
10 (M)	34 [8]		42 (27)	K		15 (9)		16 (6)
11 (M)	29 [8]		25 (17)	30 (19)				16 (5)
12 (M)	39 [6]		30 (14)	16 (7)		K	4 (0)	8 (3)
Total Neuron Count SOV-Dependent Neurons ()		295 (159)		198 (113)		270 (123)	4 (0)	88 (33)

Record & Histological validation	Record from target successfully	Record but no neuron crossing threshold (>7 std)

Table S1. Detailed recording information from brainstem-hypothalamic structures. The cells include information about which targets were recorded from successfully as well as the number of well-defined SOV-dependent and total units counted over the entire course of recordings for each axis and animal. The final row is the sum of SOV and total units over all animals in the cohort. Animals 1-5 had three Microdrive axes, animals 6-11 had a total of four microdrive axes, and animal 12 had a total of five microdrive axes. Formatting of cells refer to the following conditions: recorded units with histological validation that the electrodes hit the target (green); recorded units with no histological validation (orange). For this group the state-dependency of the unit-recordings was established based on EEG and behavioral measures; recorded activity but no units crossed the 7 SD threshold (red). Some implanted microwire bundles were kinked (K) during the Microdrive implant procedure or later driving sessions, which prevented electrodes from driving. Sessions were continuous recording periods between electrode-driving sessions. Recording sessions typically lasted between 3 and 10 days.

Characterization of neural activity during state transitions

Our main goal is to understand the role of brainstem and hypothalamic neurons in the emergence of sleep-wake states and the transitions between them. By clarifying the temporal relationship between spontaneous neuronal activity and state transitions in freely behaving animals, we can elucidate the role of specific cell-groups in the initiation or maintenance of a SOV. Therefore, we acquired simultaneous measurements of single- and multi-unit activity from a subset of the sleep-wake regulatory cell-groups as well as hippocampal LFP and ECoG.

As described in the methods, SOV and state transition times were defined from the hippocampal, cortical, and behavioral signs of the state [1], using spectral features of the hippocampal LFP, ECoG, and head acceleration.

We first examined the activity of each identified neuron during all states of vigilance. We extracted the firing rates for the identified neurons and validated their location via histological analysis. An example of these processing and analysis steps for an identified REM-active neuron in the PPT cell-group is shown in Fig. S1. The data shown are from one animal, over all IS to REM instances (n = 168) in one 5-day recording session. The histological analysis (Fig. S1A) confirmed that the electrode was in PPT. Likewise, the neuron's waveform (Fig. S1B) and inter-spike interval histogram (ISIH) is consistent with cholinergic cells of the PPT (Fig. S1C) [2–5].

Every detected spike of this particular neuron during every IS to REM transition was marked (raster plot in Fig. S1D upper panel) and the average state-conditioned firing rate, as a function of time with respect to transition time, was computed. The average state conditioned firing rate (over all REM to IS incidents) for this particular PPT neuron during both the IS and REM is shown in black traces in the bottom panel of Fig. S1D. Consistent with a REM-active neuron (one whose activity is high during REM) the average firing rate is nearly constant for times positive with respect to the transition time, which is consistent with the raster-plot having consistent firing in the green-

778 shaded regions (Fig. S1D upper panel). Note that the variance in firing rate goes up for large
779 time periods because there are fewer very long REM periods over which it is calculated.

780 To calculate changes in firing rate during state transitions, we used Poisson statistics. The pre-
781 transition average firing rate over many trials formed the reference distribution. An example of the
782 mean of the average firing rate distribution during the all the ISs is indicated by the solid dashed
783 line in the lower panel of Fig. S1D. We then used the cumulative distribution function with 1%-
784 99% confidence intervals to find the post-transition instantaneous firing rate outside of the
785 confidence bounds. The time point associated with the significantly different instantaneous firing
786 rate was then determined as t_{sig}. The orange dashed line in the lower panel of Fig. S1D indicated
787 the t_{sig} for this specific neuron.

788 In addition to the state-conditioned firing rates, we simultaneously compute and report the
789 probability of being in a state, P(state). The green and magenta lines in the bottom panel of
790 Fig. S1D indicate the P(IS) and P(REM). By construction, according to the homeostatic sleep
791 drive, once the dynamics transition into a state, the probability of staying in that state
792 monotonically decreases over time. The P(state) shown in Fig. S1D is an example of this
793 phenomenon, where the P(REM) monotonically decreases during time spent in REM.

794 The procedural steps detailed in Fig. S1 for one PPT neuron were implemented to collect the
795 state-conditioned firing rates and P(state) for all identified neurons as well as for all periods before
796 and after every allowed transition type.

797

798

799

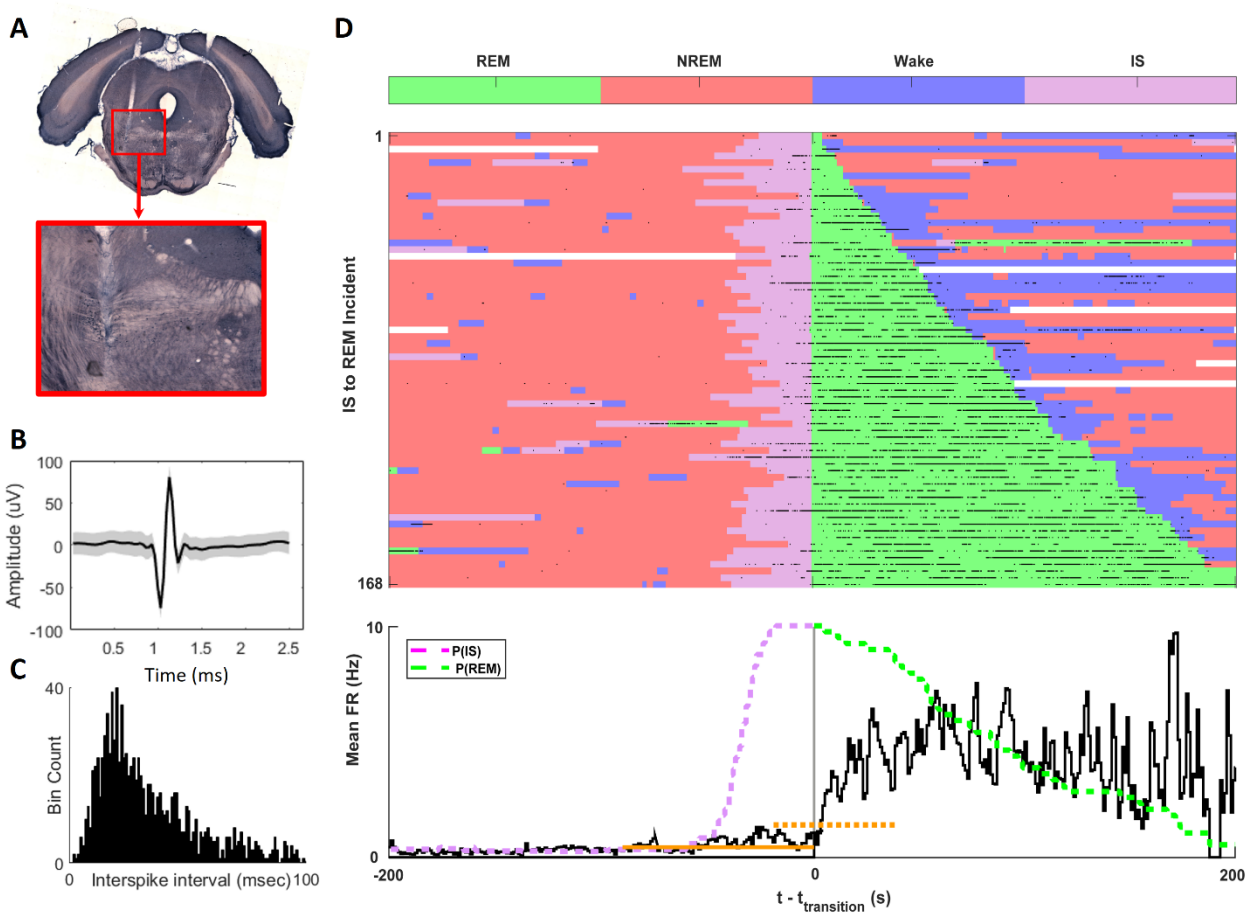

Figure S1. Activity analysis of a representative REM-active PPT neuron. **(A)** NADPH-stained coronal section of the brain show the cholinergic population in the PPT as well as the electrode track in the PPT. **(B)** Average waveform of the identified action potential for one PPT neuron over one 5-day long driving session. **(C)** The inter-spike interval (ISI) of the neuron. **(D)** Peri-REM firing rate of a PPT neuron in one animal. The raster plot is ranked according to the duration of REM bouts and with respect to time since transition into REM. The firing activity of the neuron is indicated by the black markers. In a raster plot format they each indicate every time an action potential is recorded. We calculated the probability of each state given time from state onset; indicated by the dashed lines in the bottom panel (magenta for IS; P(IS) and green for REM; P(REM)). On average, the PPT neuron fires much more infrequently during the IS bout, and only significantly increases its activity during REM (green area). The significance is calculated based

812 on the Poisson statistics, where the reference firing rate distribution is the average firing rate of
813 the prior state (here, IS) over many trials indicated by the solid orange line. The time point when
814 the instantaneous firing rate falls out of the 1%-99% confidence bounds is marked as t_{sig} marked
815 here by the orange dashed line. As P(REM) decays, so does the average firing rate. The average
816 firing rate here indicates the neuronal activity conditioned on state and is calculated in 1 second
817 bins. The probability traces are rescaled from [0,1] to [0,10] to match the scale of the average
818 firing rate.

819

820

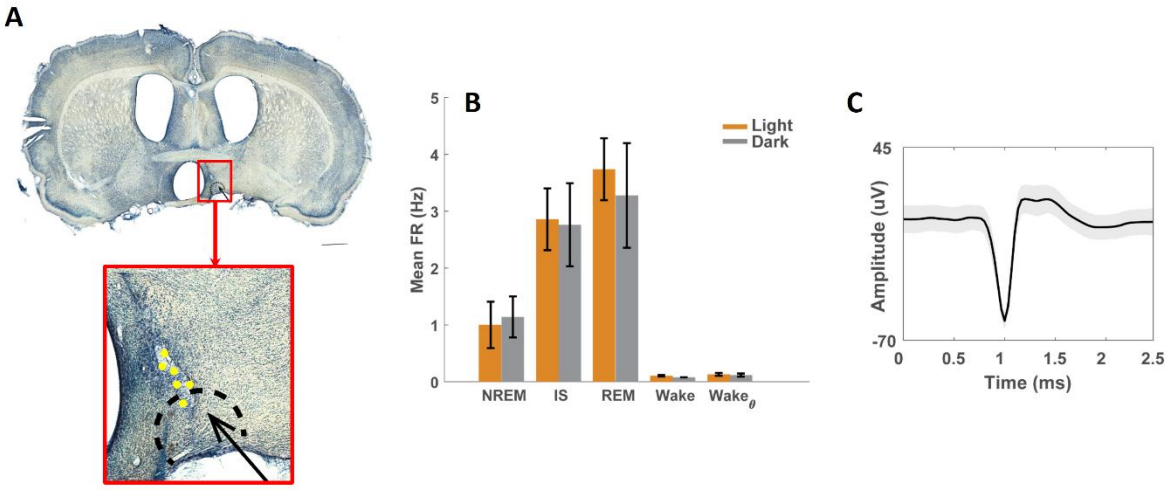

Figure S2. Identified neurons in lateral hypothalamus are active during the intermediate state. A group of neurons were identified on route to VLPO. **(A)** Example locations on the electrode track where these IS-active neurons were recorded are indicated by yellow markers. **(B)**These neurons are active during REM and IS bouts and increase their firing rate slightly upon transitions from IS to REM. However they are off during Wake. Based on histological analysis, their activity, and their average waveform **(C)** these neurons might be the ones in lateral hypothalamus that are shown to contain melatonin-concentrating hormone.

1. Datta, S. & MacLean, R. R. Neurobiological mechanisms for the regulation of mammalian sleep–wake behavior: reinterpretation of historical evidence and inclusion of contemporary cellular and molecular evidence. *Neurosci. Biobehav. Rev.* **31**, 775–824 (2007).

2. Grace, K. P., Vanstone, L. E. & Horner, R. L. Endogenous Cholinergic Input to the Pontine REM Sleep Generator Is Not Required for REM Sleep to Occur. *J. Neurosci.* **34**, 14198–14209 (2014).

3. Satoh, K. & Fibiger, H. C. Cholinergic neurons of the laterodorsal tegmental nucleus: Efferent and afferent connections. *J. Comp. Neurol.* (1986). doi:10.1002/cne.902530302

4. Van Dort, C. J. *et al.* Optogenetic activation of cholinergic neurons in the PPT or LDT induces REM sleep. *Proc. Natl. Acad. Sci.* (2015). doi:10.1073/pnas.1423136112

5. Datta, S. & Siwek, D. F. Single cell activity patterns of pedunculopontine tegmentum neurons across the sleep-wake cycle in the freely moving rats. *J. Neurosci. Res.* **70**, 611–621 (2002).